Journal of Science and Transport Technology
Journal homepage: https://jstt.vn/index.php/en

Nonlinear buckling and postbuckling of FG-CNTRC sandwich plates with multi-layer corrugated FG-CNTRC core

Vu Minh Duc[1,2], Do Thi Kieu My[3,4,*], Vu Hoai Nam[5]

[1]Laboratory of Advanced Materials and Structures, Institute for Advanced Study in Technology, Ton Duc Thang University, Ho Chi Minh City, Vietnam
[2]Faculty of Civil Engineering, Ton Duc Thang University, Ho Chi Minh City, Vietnam
[3]Institute of Transport Technology, University of Transport Technology, Hanoi, Vietnam
[4]Institute for Building Materials and Construction Protection, Institute of Transport Science and Technology, Hanoi, Vietnam
[5]Faculty of Civil Engineering, University of Transport Technology, Hanoi, Vietnam

Article info
Type of article:
Original research paper

DOI:
https://doi.org/10.58845/jstt.utt.2024.en.4.4.55-70

[*]Corresponding author:
Email address:
mydtk@utt.edu.vn

Received: 25/10/2024
Revised: 10/12/2024
Accepted: 12/12/2024

Abstract: This paper proposes an analytical solution for the nonlinear buckling behavior of functionally graded carbon nanotube-reinforced composite (FG-CNTRC) sandwich plates under axial compressive and external pressure loads is analytically examined in this paper. The considered plates are designed with the multi-layer corrugated FG-CNTRC core and face sheets. The CNT distribution laws of the multi-layer corrugated core are proposed to ensure the material continuity between FG-CNTRC face sheets and multi-layer corrugated core. Classical plate theory (CPT) with geometrical nonlinearities is utilized to formulate the fundamental expressions. In addition, the Ritz energy method is used to achieve the expressions of compression and pressure postbuckling curves, and axial critical buckling loads. The investigations numerically display the influences of multi-layer corrugated core, material, and geometrical properties on the nonlinear buckling and postbuckling behavior of plates.

Keywords: Ritz energy method, Classical plate theory, Functionally graded carbon nanotube-reinforced composite, Buckling and postbuckling, Multi-layer corrugated core.

1. Introduction

Over the past twenty years, the investigation of the mechanic behavior of beams, plates, and shells manufacted by advanced sandwich composites has been an active research focus. The researches of the structural behavior composed of soft-core sandwich materials, with load-bearing surface layers made of advanced composites such as functionally graded material (FGM), has attracted considerable interest from researchers worldwide, with various methods being applied. Using classical plate theory (CPT) combined with von Karman nonlinear geometrical terms, the Galerkin method, and the stress approach, Singh and Harha [1] analyzed the nonlinear dynamic responses of FGM sandwich plates placed on elastic foundation in a thermal environment. Sobhy [2] used an advanced plate theory with shear strains to study the vibration and buckling behavior of FGM sandwich plates in a hygrothermal environment. The thermal buckling behavior of different FGM sandwich plate configurations was examined by Zenkour and Sobhy [3]. Subsequently, by applying the improved mesh-free method with radial point interpolation, Vuong and Lee [4] analyzed the thermal buckling behavior of FGM sandwich plates. For the shell problems, stiffened FGM sandwich doubly curved shells were investigated by Dong and Dung [5] in nonlinear vibration problems, using Lekhnitskii's smeared stiffener technique, higher-order shear deformation theory, Galerkin method, and Runge-Kutta method, with four material types. Nam et al. [6, 7] studied the buckling and postbuckling behavior of porous cylindrical shells with FGM coatings, as well as FGM sandwich cylindrical shells in a thermal environment, stiffened by spiral stiffeners, under torsional loading. The Galerkin method combined with the closed circumferential condition of the cylindrical shell was applied, and the selected solution of deflection was chosen in the three-term form, allowing for the analysis of three stages: pre-buckling, linear buckling, and nonlinear buckling.

In recent decades, due to their exceptional mechanical, thermal, and electrical properties, carbon nanotube (CNT) has attracted significant attention. These attributes make CNTs highly promising for use in advanced composite structures, where their ability to enhance strength and stiffness while maintaining lightweight properties. Consequently, research efforts have increasingly focused on optimizing the performance of CNT-reinforced composites. Moreover, their high aspect ratio further positions CNTs as ideal filler materials for advanced composite. Expanding on the concept of functionally graded materials (FGMs), Shen [8] introduced an advanced composite material, which is functionally graded carbon nanotube-reinforced composite (FG-CNTRC). In this composite, an isotropic matrix is reinforced by CNTs, continuously distributed along the thickness direction, allowing for optimized structural responses and improved performance based on specific design requirements. Motivated by this suggestion, sequential works relating to the static stability of FG-CNTRC structures have been performed. The linear buckling problems of FG-CNTRC plates subjected to mechanic loads was investigated in studies [9, 10] using numerical and semi-analytical methods, respectively. Shen and Xiang [11] and Liew et al. [12] explored the axially compressed buckling and postbuckling behavior of FG-CNTRC cylindrical panels. By considering temperature-dependent material properties and transversely flexible core, Mohammadimehr and Mostafavifar [13] examined the free vibrations of FG-CNTRC sandwich plates in magnetic field, by employing strain gradient theory. In thermally postbuckled state, Shen et al. [14] investigated the vibrations of FG-CNTRC sandwich plates on elastic foundation. Di Sciuva and Sorrenti [15] studied the free vibration and buckling of FG-CNTRC sandwich plates utilizing the extended refined zigzag theory. Based on higher-order shear deformation theory, FG-CNTRC sandwich annular plates were investigated by Ansari et al. [16] in nonlinear axisymmetric vibrations. By using the Carrera unified formulation, Beni [17] conducted free vibrations of annular sector FG-CNTRC sandwich plates. The vibrations of doubly curved smart FG-CNTRC sandwich shells with porous cores were presented by Setoodeh et al. [18], and Wang et al. [19] investigated similar behavior with solid cores. Besides FG-CNTRC structures, functionally graded graphene-reinforced composite (FG-GRC) sandwich structures are also a topic of great interest currently. It can be observed that there are very few studies on this structure worldwide; for example, the nonlinear vibration was investigated by Wang and Shen [20] for FG-GRC sandwich plates in thermal environment.

For corrugated structures, many authors worldwide have researched using various theories and approaches. Samanta and Mukhopadhyay [21] analyzed the mechanical response of trapezoidal corrugation plates, taking into account both bending and extensional stiffness. Peng et al. [22] proposed an equivalent elastic property theory for sinusoidal and trapezoidal corrugated plates using the meshless Galerkin method. The corrugated composites with special mechanic properties were applied for flexible wing structures as indicated by Yokozeki et al. [23]. More recently, Hieu et al. [24] examined the elastic stability of isotropic trapezoidal corrugated metal piping without elastic foundations using Donnell shell theory and the homogenization approach of Samanta and Mukhopadhyay [21]. Kavermann and Bhattacharyya [25] conducted experimental studies on the static annalysis of corrugated plywood sandwich cores, Shaban and Alibeigloo [26] employed the energy method to solve the three-dimensionally elastic problem of sandwich panels with corrugated core. Two-layer corrugated sandwich panels were mentioned by Shu et al. [27] using the crashworthiness analysis with crushing loads, and Zamanifar et al. [28] utilized the finite strip method to investigate the dynamic and static behavior of corrugated-core sandwich plates. By applying the homogenization technique of Xia et al. [29], Nam et al. [30] studied the nonlinear thermo-elastic stability of FG-CNTRC sandwich cylindrical shells with corrugated core under radial pressure, My et al. [31] explored the nonlinear buckling responses of FG-GRC sandwich toroidal shell segments in thermal environment with corrugated cores under lateral pressure.

An analytical approach for buckling and postbuckling behavior of FG-CNTRC sandwich plates with a corrugated FG-CNTRC core, utilizing CPT is introduced in this paper. Through the application of the Ritz energy method, the axial critical buckling loads and postbuckling curves of the plates are explicitly derived. The influence of material and geometric parameters of the FG-CNTRC face sheets and the corrugated core on the buckling and postbuckling performance is illustrated by numerical examples.

2. Theoretical formulations

This paper investigates FG-CNTRC sandwich plates with a multi-layer corrugated FG-CNTRC core subjected to axial compression P_0 and external pressure q in a thermal environment T. The geometrical and material properties, and coordinate system of the plates, corrugated FG-CNTRC core, and FG-CNTRC face sheets can be referred to in Figs. 1 and 2. The corrugated core is considered to be in the trapezoidal and round forms. The length and width of the plates are denoted as a and b, respectively. The thickness of the FG-CNTRC face sheet is represented by h_f, h_c; and h denote the core thickness and the total thickness, respectively. c and t represent the half-period and the wall thickness of the corrugation, respectively. For round corrugations, r represents the radius of the half-corrugation, and d denotes the half-length of the line connecting two adjacent half-corrugations. In the case of trapezoidal corrugations, θ and f represent the trough angle and the half-amplitude of the corrugation, respectively.

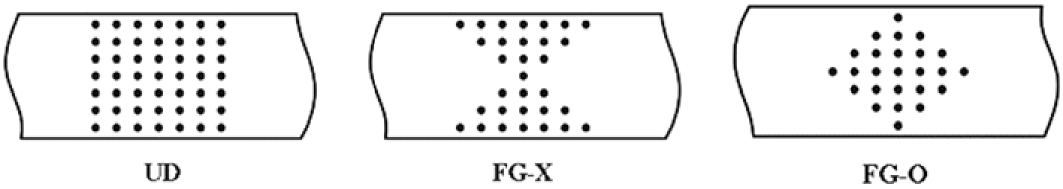

Fig. 1. CNT distributions in corrugated core and face sheets

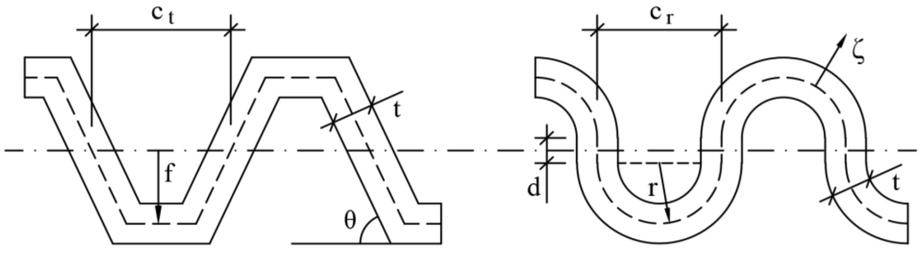

Trapezoidal corrugated core

Round corrugated core

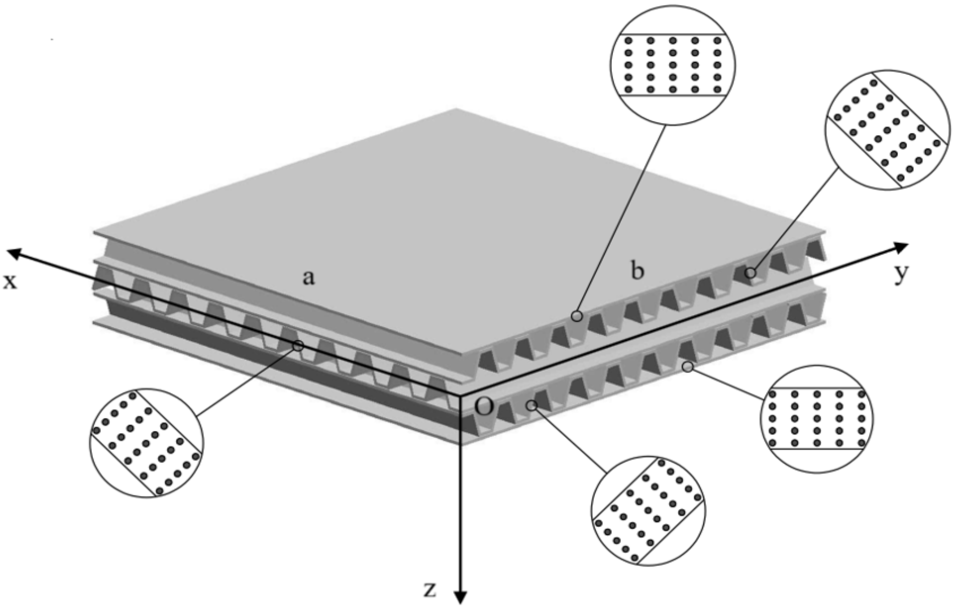

Fig. 2. Coordinate systems and geometry of FG-CNTRC sandwich plates and corrugated FG-CNTRC cores

The CNTs in the face sheets can be designed in the longitudinal (x-directional CNT face sheets, 0-layer) or transversal (y-directional CNT face sheets, 90-layer) directions of the plates and the CNTs in the corrugated core are always in the same direction as the corrugations, while, the corrugated may be in the longitudinal (0-layer) or transversal (90-layer) directions of the plates. Four combination cases of CNT directions are considered as follows: 0/0/90/0/0 plates, 0/90/0/90/0 plates, 90/0/90/0/90 plates, 90/90/0/90/90 plates.

The upper face sheet $\left(-\frac{h}{2} \le z \le -\frac{h_c}{2}\right)$ is reinforced by CNT, with distributions in the thickness according to the following functions

UD law:

$$V_{CNT} = V_{CNT}^{*}, \tag{1}$$

FG-X law:

$$V_{CNT} = \left|\frac{8z + 2h + 2h_c}{h - h_c}\right| V_{CNT}^{*}, \tag{2}$$

FG-O law:

$$V_{CNT} = \left(2 - \left|\frac{8z + 2h + 2h_c}{h - h_c}\right|\right) V_{CNT}^{*}, \tag{3}$$

and for the lower face sheet $\left(\frac{h_c}{2} \le z \le \frac{h}{2}\right)$, CNT volume fractions are distributed according to the following functions

UD law:

$$V_{CNT} = V_{CNT}^{*}, \tag{4}$$

FG-X law:

$$V_{CNT} = \left|\frac{8z - 2h - 2h_c}{h - h_c}\right| V_{CNT}^{*}, \tag{5}$$

FG-O law:

$$V_{CNT} = \left(2 - \left|\frac{8z - 2h - 2h_c}{h - h_c}\right|\right) V_{CNT}^{*}, \tag{6}$$

Additionally, the CNT volume fractions for the corrugated core $\left(-\frac{t}{2}\leq\zeta\leq\frac{t}{2}\right)$ are proposed to be linearly distributed through the thickness of the core wall according to the following functions, as

UD law:

$$V_{CNT}=V_{CNT}^{*}, \tag{7}$$

FG-X law:

$$V_{CNT}=\left(\frac{4\zeta}{t}\right)V_{CNT}^{*}, \tag{8}$$

FG-O law:

$$V_{CNT}=\left(2-\frac{4\left|\zeta\right|}{t}\right)V_{CNT}^{*}. \tag{9}$$

where ζ is the thickness direction axis of the corrugation wall in the local coordinate systems of corrugation.

To forecast the elastic constants, the extended mixture rule is adopted. The formulations of Poison ratio, shear modulus, and Young's moduli are presented by

$$\begin{aligned}
&E_{11}=V_mE_m+\mu_1V_{CNT}E_{11}^{CNT},\\
&E_{22}=\frac{\mu_2E_mE_{22}^{CNT}}{V_{CNT}E_m+V_mE_{22}^{CNT}},\\
&G_{12}=\frac{\mu_3G_mG_{12}^{CNT}}{G_mV_{CNT}+V_mG_{12}^{CNT}},\\
&\nu_{12}=V_m\nu_m+V_{CNT}^{*}\nu_{12}^{CNT},
\end{aligned} \tag{10}$$

where V_{CNT} and V_m (satisfies the relation of $V_{CNT}+V_m=1$) denotes the CNT and matrix volume fractions. The CNT Young's moduli and shear modulus are defined by E_{11}^{CNT}, E_{22}^{CNT} and G_{12}^{CNT}. The corresponding attributives for the matrix are denoted by E_m and G_m; ν_{12}^{CNT} and ν_m are the CNT and matrix Poisson's ratios, and the CNT efficiency parameters $\mu_j\left(j=1,\ 2,\ 3\right)$ are determined by Molecular Dynamics (MD) emulations [32-34].

In the x- and y-directions, the thermal expansion coefficients are determined as

$$\begin{aligned}
&\alpha_{11}=V_{CNT}\alpha_{11}^{CNT}+V_m\alpha_m,\\
&\alpha_{22}=\left(1+\nu_{12}^{CNT}\right)V_{CNT}\alpha_{22}^{CNT}\\
&\qquad+\left(1+\nu_m\right)V_m\alpha_m-\nu_{12}\alpha_{11},
\end{aligned} \tag{11}$$

where the CNT and matrix coefficients of thermal expansion are denoted by α_{11}^{CNT}, α_{22}^{CNT} and α_m, respectively.

For the orthotropic plates, Hooke's law can be presented by

$$\begin{bmatrix}\sigma_x\\ \sigma_y\\ \sigma_{xy}\end{bmatrix}=\begin{bmatrix}Q_{11}&Q_{12}&0\\ Q_{12}&Q_{22}&0\\ 0&0&Q_{66}\end{bmatrix}\left(\begin{bmatrix}\varepsilon_x\\ \varepsilon_y\\ \gamma_{xy}\end{bmatrix}-\begin{bmatrix}\alpha_{11}\\ \alpha_{22}\\ 0\end{bmatrix}\Delta T\right), \tag{12}$$

where Q_{ij} is the reduced stiffnesses, determined by

$$Q_{11}=\frac{E_{11}}{1-\nu_{21}\nu_{12}},\ Q_{22}=\frac{E_{22}}{1-\nu_{21}\nu_{12}},$$

$$Q_{12}=\frac{\nu_{21}E_{11}}{1-\nu_{21}\nu_{12}},\ Q_{66}=G_{12}.$$

The force and moment resultants of FG-CNTRC plates with corrugated FG-CNTRC cores are obtained by integrating Hooke's law in the thickness direction and combining with the homogenization technique of Xia et al. [29], presented by

$$\begin{Bmatrix}N_x\\ N_y\\ N_{xy}\\ M_x\\ M_y\\ M_{xy}\end{Bmatrix}=\begin{bmatrix}A_{11}&A_{12}&0&0&0&0\\ A_{12}&A_{22}&0&0&0&0\\ 0&0&A_{66}&0&0&0\\ 0&0&0&D_{11}&D_{12}&0\\ 0&0&0&D_{12}&D_{22}&0\\ 0&0&0&0&0&D_{66}\end{bmatrix}\begin{Bmatrix}\varepsilon_x^0\\ \varepsilon_y^0\\ \gamma_{xy}^0\\ -w_{,xx}\\ -w_{,yy}\\ -2w_{,xy}\end{Bmatrix}-\begin{Bmatrix}\Phi_{1x}\\ \Phi_{1y}\\ 0\\ 0\\ 0\\ 0\end{Bmatrix}, \tag{13}$$

where the stiffnesses of FG-CNTRC plates A_{ij} and D_{ij} are determined by summing the stiffnesses of two FG-CNTRC face sheets and the multi-layer corrugated FG-CNTRC core, presented as

$$\begin{gathered}\left(A_{ij},D_{ij}\right)=\left(A_{ij}^{upper},D_{ij}^{upper}\right)\\+\left(A_{ij}^{[1]c},D_{ij}^{[1]c}\right)+\left(A_{ij}^{[2]c},D_{ij}^{[2]c}\right)\\+\left(A_{ij}^{[3]c},D_{ij}^{[3]c}\right)+\left(A_{ij}^{lower},D_{ij}^{lower}\right),\\\left(\Phi_{1x},\Phi_{1y}\right)=\left(\Phi_{1x}^{upper},\Phi_{1y}^{upper}\right)\\+\left(\Phi_{1x}^{[1]c},\Phi_{1y}^{[1]c}\right)+\left(\Phi_{1x}^{[2]c},\Phi_{1y}^{[2]c}\right)\\+\left(\Phi_{1x}^{[3]c},\Phi_{1y}^{[3]c}\right)+\left(\Phi_{1x}^{lower},\Phi_{1y}^{lower}\right),\end{gathered}\tag{14}$$

for the face sheets

$$\left(A_{ij}^{upper},D_{ij}^{upper}\right)=\int_{-\frac{h}{2}}^{-\frac{h_c}{2}}Q_{ij}^{up}\left(1,z^2\right)dz,$$

$$\left(A_{ij}^{lower},D_{ij}^{lower}\right)=\int_{\frac{h_c}{2}}^{\frac{h}{2}}Q_{ij}^{lo}\left(1,z^2\right)dz,$$

$$\left(i,j\right)=\left(1,2,6\right),$$

$$\Phi_{1x}^{upper}=\int_{-\frac{h}{2}}^{-\frac{h_c}{2}}\left(Q_{11}^{up}\alpha_{11}^{up}+Q_{12}^{up}\alpha_{22}^{up}\right)dz,$$

$$\Phi_{1x}^{lower}=\int_{\frac{h_c}{2}}^{\frac{h}{2}}\left(Q_{11}^{lo}\alpha_{11}^{lo}+Q_{12}^{lo}\alpha_{22}^{lo}\right)dz,$$

$$\Phi_{1y}^{upper}=\int_{-\frac{h}{2}}^{-\frac{h_c}{2}}\left(Q_{12}^{up}\alpha_{11}^{up}+Q_{22}^{up}\alpha_{22}^{up}\right)dz,$$

$$\Phi_{1y}^{lower}=\int_{\frac{h_c}{2}}^{\frac{h}{2}}\left(Q_{12}^{lo}\alpha_{11}^{lo}+Q_{22}^{lo}\alpha_{22}^{lo}\right)dz,$$

and for 3 layers of corrugated core, the components of the stiffness matrix $A_{ij}^{[1]c},A_{ij}^{[2]c},A_{ij}^{[3]c},D_{ij}^{[1]c},D_{ij}^{[2]c},D_{ij}^{[3]c}$ and $\Phi_{1x}^{[1]c},\Phi_{1x}^{[2]c},\Phi_{1x}^{[3]c},\Phi_{1y}^{[1]c},\Phi_{1y}^{[2]c},\Phi_{1y}^{[3]c}$ are defined as follows

- for x-directional corrugated core

$$\begin{aligned}&A_{22}^{[k]c}=\frac{2c}{\dfrac{l_1}{\bar{A}_{11}}+\dfrac{l_2}{\bar{D}_{11}}},\\&A_{12}^{[k]c}=\frac{A_{22}^{[k]c}\bar{A}_{12}}{\bar{A}_{11}},\\&A_{11}^{[k]c}=\frac{l}{c}\frac{\bar{A}_{11}\bar{A}_{22}-\bar{A}_{12}^2}{\bar{A}_{11}}+\frac{A_{12}^{[k]c}\bar{A}_{12}}{\bar{A}_{11}},\\&A_{66}^{[k]c}=\frac{c}{l}\bar{A}_{66},\\&D_{22}^{[2]c}=\frac{c}{l}\bar{D}_{11},\\&D_{12}^{[2]c}=\frac{\bar{D}_{12}}{\bar{D}_{11}}D_{22}^{[2]c},\\&D_{11}^{[2]c}=\frac{1}{2c}\left(l_2\bar{A}_{22}+l_1\bar{D}_{22}\right),\\&D_{66}^{[2]c}=\frac{l}{c}\bar{D}_{66},\\&D_{ij}^{[1]c}=\int_{-\frac{h_c}{2}}^{-\frac{h_c}{6}}Q_{ij}^{*c}z^2dz,\ D_{ij}^{[3]c}=\int_{\frac{h_c}{6}}^{\frac{h_c}{2}}Q_{ij}^{*c}z^2dz,\\&\Phi_{1x}^{[k]c}=A_{11}^{[k]c}\bar{\alpha}_{11}^{c}+A_{12}^{[k]c}\bar{\alpha}_{22}^{c},\\&\Phi_{1y}^{[k]c}=A_{12}^{[k]c}\bar{\alpha}_{11}^{c}+A_{22}^{[k]c}\bar{\alpha}_{22}^{c},\\&k=\left(1,2,3\right),\end{aligned}\tag{15}$$

- for y-directional corrugated core

$$\begin{aligned}&A_{11}^{[k]c}=\frac{2c}{\dfrac{l_1}{\bar{A}_{11}}+\dfrac{l_2}{\bar{D}_{11}}},\\&A_{12}^{[k]c}=\frac{A_{11}^{[k]c}\bar{A}_{12}}{\bar{A}_{11}},\\&A_{22}^{[k]c}=\frac{l}{c}\frac{\bar{A}_{11}\bar{A}_{22}-\bar{A}_{12}^2}{\bar{A}_{11}}+\frac{A_{12}^{[k]c}\bar{A}_{12}}{\bar{A}_{11}},\end{aligned}\tag{16}$$

$$A_{66}^{[k]c}=\frac{c}{l}\bar{A}_{66},$$

$$D_{11}^{[2]c}=\frac{c}{l}\bar{D}_{11},$$

$$D_{12}^{[2]c}=\frac{\bar{D}_{12}}{\bar{D}_{11}}D_{11}^{[2]c},$$

$$D_{22}^{[2]c}=\frac{1}{2c}\left(l_2\bar{A}_{22}+l_1\bar{D}_{22}\right),$$

$$D_{66}^{[2]c}=\frac{l}{c}\bar{D}_{66},$$

$$D_{ij}^{[1]c}=\int_{-\frac{h_c}{2}}^{-\frac{h_c}{6}}Q_{ij}^{*c}z^2dz,\; D_{ij}^{[3]c}=\int_{\frac{h_c}{6}}^{\frac{h_c}{2}}Q_{ij}^{*c}z^2dz,$$

$$\Phi_{1y}^{[k]c}=A_{11}^{[k]c}\bar{\alpha}_{11}^{c}+A_{12}^{[k]c}\bar{\alpha}_{22}^{c},$$

$$\Phi_{1x}^{[k]c}=A_{12}^{[k]c}\bar{\alpha}_{11}^{c}+A_{22}^{[k]c}\bar{\alpha}_{22}^{c},$$

$$k=\left(1,2,3\right),$$

in which

- for trapezoidal corrugations

$$c=c_t,$$

$$l=\left(\frac{1}{\sin\theta}-\frac{1}{\tan\theta}\right)2f+c,$$

$$l_1=-\frac{\cos\theta}{3\sin\theta}8f+2c,$$

$$l_2=f^2\left(2c-4\frac{f}{\tan\theta}\right)+\frac{4f^3}{3\sin\theta},$$

- for round corrugations

$$l=2d+r\pi,$$

$$c=c_r=2r,$$

$$l_1=r\pi,$$

$$l_2=2\pi d^2r+r^3\pi+8dr^2+\frac{4d^3}{3}.$$

and

$$\left(\bar{A}_{ij},\bar{D}_{ij}\right)=\int_{-\frac{t}{2}}^{\frac{t}{2}}Q_{ij}^{c}\left(1,\zeta^2\right)d\zeta,$$

$$\left(\bar{\alpha}_{11}^{c},\bar{\alpha}_{22}^{c}\right)=\frac{1}{t}\int_{-\frac{t}{2}}^{\frac{t}{2}}\left(\alpha_{11},\alpha_{22}\right)d\zeta,$$

$$Q_{ij}^{*c}=\frac{12}{\left(\frac{h_c}{3}\right)^3}D_{ij}^{[2]c}, \qquad (17)$$

Note that: The stiffnesses $D_{ij}^{[2]c}$ in Eq. (17) are determined from Eq. (15) for 1st and 3rd for y-directional corrugated cores, oppositely, from Eq. (16) for 1st and 3rd for x-directional corrugated cores.

The compatibility equation of the plates according to the CPT is also applied as [30]

$$\begin{aligned}-\gamma_{xy,xy}^{0}+\varepsilon_{y,xx}^{0}+\varepsilon_{x,yy}^{0}&=-w_{,xx}-w_{,xx}w_{,yy}^{*}-w_{,xx}w_{,yy}\\&+w_{,xy}^{2}-w_{,xx}^{*}w_{,yy}+2w_{,xy}w_{,xy}^{*}.\end{aligned} \qquad (18)$$

The stress function $f\left(x,y\right)$ is introduced, with the following conditions

$$N_{xy}=-f_{,xy},\; N_x=f_{,yy},\; N_y=f_{,xx}. \qquad (19)$$

The boundary conditions of the plates are assumed to be simply supported and freely movable edges, as

$$\begin{aligned}&M_x\big|_{x=0,a}=0,\; w\big|_{x=0,a}=0,\; N_{xy}\big|_{x=0,a}=0,\\&N_x=N_{0x}=-hP_0,\\&N_{xy}\big|_{y=0,b}=0,\; w\big|_{y=0,b}=0,\; M_y\big|_{y=0,b}=0,\\&N_y=N_{0y}=0,\end{aligned} \qquad (20)$$

In this case, the approximate solutions of deflection and imperfection are presented in the forms, as

$$\begin{aligned}&w=W\sin\alpha x\sin\beta y,\\&w^{*}=\xi h\sin\alpha x\sin\beta y,\end{aligned} \qquad (21)$$

where $\alpha=\frac{m\pi}{a}$, $\beta=\frac{n\pi}{b}$; m and n are the buckling modes.

The compatibility equation (18) is rewritten by

$$A_{22}^{*}f_{,xxxx}+\left(2A_{12}^{*}+A_{66}^{*}\right)f_{,xxyy}$$
$$+w_{,xx}w_{,yy}+w_{,xx}-2w_{,xy}w_{,xy}^{*} \qquad (22)$$
$$+A_{11}^{*}f_{,yyyy}+w_{,xx}^{*}w_{,yy}+w_{,xx}w_{,yy}^{*}-w_{,xy}^{2}=0.$$

where

$$A_{11}^{*}=\frac{A_{22}}{A_{11}A_{22}-A_{12}^{2}},\ A_{12}^{*}=\frac{-A_{12}}{A_{11}A_{22}-A_{12}^{2}},$$

$$A_{22}^{*}=\frac{A_{11}}{A_{11}A_{22}-A_{12}^{2}},$$

$$A_{66}^{*}=\frac{1}{A_{66}},$$

By substituting the solution forms Eq. (21) into the compatibility equation (22), the stress function can be derived and expressed as follows

$$f=f_1\cos 2\alpha x+f_2\cos 2\beta y$$
$$+f_3\sin\alpha x\sin\beta y+\frac{N_{0y}x^2}{2}+\frac{N_{0x}y^2}{2}. \qquad (23)$$

The strain energy of the plates and the work done by the external loads are expressed by

$$U_{in}=\frac{1}{2}\int_{-\frac{h}{2}}^{\frac{h}{2}}\int_{0}^{b}\int_{0}^{a}\left[\sigma_y\left(\varepsilon_y-\alpha_{22}\Delta T\right)+\sigma_x\left(\varepsilon_x-\alpha_{11}\Delta T\right)+\sigma_{xy}\gamma_{xy}\right]dxdydz \qquad (24)$$

$$U_{ext}=-\int_{0}^{b}\int_{0}^{a}\left[\frac{1}{2}w\left(wK_1-\left(w_{,yy}+w_{,xx}\right)K_2+\frac{w^3}{2}K_3\right)\right]dxdy+\int_{0}^{b}\int_{0}^{a}qwdxdy+N_{0x}\int_{0}^{b}\int_{0}^{a}u_{,x}dxdy \qquad (25)$$

where K_1,K_2 are the linear foundation stiffnesses and K_3 is the stiffness of the nonlinear foundation.

The total potential energy is established by

$$U_{total}=U_{in}-U_{ext}. \qquad (26)$$

The Ritz energy method is applied, as

$$\frac{\partial U_{total}}{\partial W}=0, \qquad (27)$$

leads to

$$H_{11}W+H_{12}W\left(W+\frac{4}{3}\xi h\right)$$
$$+H_{13}W\left(2h\xi+W\right)\left(h\xi+W\right) \qquad (28)$$
$$+H_{14}W^3K_3+H_{15}q-H_{16}P_0h\left(h\xi+W\right)=0$$

where

$$H_{11}=\frac{ab}{4}\left\{\begin{array}{l}\left(A_{22}^{*}X_{31}{}^{2}+D_{11}\right)\alpha^4+\left[X_{31}{}^{2}\left(2A_{12}^{*}+A_{66}^{*}\right)+2D_{12}+4D_{66}\right]\beta^2\alpha^2\\ +\left(A_{11}^{*}X_{31}{}^{2}+D_{22}\right)\beta^4+\left(\alpha^2+\beta^2\right)K_2+K_1\end{array}\right\},$$

$$H_{12}=-\frac{4\delta_n\delta_mX_{31}}{\alpha\beta}\left[X_{11}A_{22}^{*}\alpha^4+A_{12}^{*}\left(X_{11}+X_{21}\right)\alpha^2\beta^2+X_{21}A_{11}^{*}\beta^4\right],$$

$$H_{13}=16ab\left(X_{11}{}^{2}\alpha^4A_{22}^{*}+X_{21}{}^{2}\beta^4A_{11}^{*}\right),$$

$$H_{14}=\frac{9ab}{64},\ \ H_{15}=-\frac{\delta_m\delta_n}{\alpha\beta},\ \ H_{16}=\frac{ab\alpha^2}{4}.$$

For the case of a plate under axial compressive load P_0, from equation (28), can obtain

$$P_0=\frac{H_{11}W+H_{12}Wh\left(W+\frac{4}{3}\xi\right)+H_{13}Wh^2\left(2\xi+W\right)\left(\xi+W\right)+H_{14}W^3h^2K_3+\frac{H_{15}q}{h}}{H_{16}h\left(\xi+W\right)} \qquad (29)$$

For the perfect plates, the static buckling loads are achieved by applying $W\rightarrow 0$, and $\xi=0$, as

$$P_0^{upper}=\frac{H_{11}}{H_{16}h} \qquad (30)$$

In the case of the plate under external pressure q, from equation (28), can obtain

$$q=-\frac{H_{11}W+H_{12}Wh\left(W+\frac{4}{3}\xi\right)+H_{13}Wh^2\left(2\xi+W\right)\left(\xi+W\right)+H_{14}W^3h^2K_3-H_{16}P_0h\left(\xi+W\right)}{\frac{H_{15}}{h}} \quad (31)$$

3. Results and disscussions

3.1. Validation

This section validates the critical axial buckling compression of FG-CNTRC plates calculated using the present method by comparing it with the results of Shen and Zhu [35] (refer to Table 1). As observed, the results show strong agreement, with the present values aligning closely with the previous ones.

3.2. Numerical examples and disscussions

For the equivalent non-corrugated plates, the thickness of the non-corrugated core can be determined with the volumes of the equivalent non-corrugated cores being equal to those of the corrugated cores, respectively, leading to the volume fractions of CNT and matrix of these two cases being the same.

Table 2 presents the effects of CNT volume fraction, directions of CNT in the face sheets and the corrugated core, and distribution types of CNT on the critical buckling compressive load of FG-CNTRC multilayer corrugated core plates. Naturally, the critical load is smallest when the CNT volume fraction $V_{CNT}^*=0.12$ and largest when $V_{CNT}^*=0.28$, for all directions and distribution types of CNT. Notably, the 0/0/90/0/0 plates and 0/90/0/90/0 plates show higher critical loads than the other two. Although the differences in critical buckling loads among the plates with distribution types UD, FG-X, and FG-O are not significant, FG-X plates still show slightly higher critical loads than corresponding UD and FG-O plates. Additionally, when comparing the two forms of corrugated cores, the critical buckling loads of plates with round corrugations tend to have a higher critical buckling load than those with trapezoidal corrugations.

Table 1. Comparisons of critical axial buckling compressive load $P_0^{cr}=\frac{H_{11}b}{H_{16}}$ (in kN) of FG-CNTRC plates ($b/h=100$, $h=2$mm, $a/b=1$, $m=1$, $n=1$)

$T(K)$	V_{CNT}^*	Shen and Zhu [35]		Present	
		UD	FG-X	UD	FG-X
300	0.12	3.34	4.87	3.39	4.93
	0.17	4.96	7.23	5.00	7.27
	0.28	7.76	11.41	7.88	11.65
500	0.12	3.18	4.64	3.24	4.74
	0.17	4.71	6.90	4.76	6.98
	0.28	7.43	10.92	7.58	11.24
700	0.12	3.03	4.44	3.12	4.60
	0.17	4.49	6.59	4.58	6.77
	0.28	7.12	10.44	7.36	10.96

Table 2. Effects of different directions of CNT in the face sheets, of CNT in the corrugated core on the critical buckling compressive loads of plates with multi-layer corrugated FG-CNTRC core (MPa) ($a = b = 100h$, $h_f = 3mm$, $h_c = 15mm$, $f = 2mm$, $c_t = 4f$, $\theta = \pi/4$, $r = 1.4mm$, $c_r = 2r$, $d = 0.6mm$, $t = 1mm$, $T = 400K$, $K_1 = 0\ MN/m^3$, $K_2 = 0\ MN/m$, $K_3 = 0\ MN/m^5$)

Directions of CNT	Trapezoidal corrugated cores			Round corrugated cores		
	UD	FG-X	FG-O	UD	FG-X	FG-O
	$V^*_{CNT} = 0.12$					
0/0/90/0/0	6.06 (1,1)*	6.10 (1,1)	6.04 (1,1)	6.31 (1,1)	6.34 (1,1)	6.28 (1,1)
0/90/0/90/0	6.06 (1,1)	6.10 (1,1)	6.04 (1,1)	6.31 (1,1)	6.34 (1,1)	6.28 (1,1)
90/0/90/0/90	5.10 (2,1)	5.14 (2,1)	5.07 (2,1)	6.04 (2,1)	6.08 (2,1)	6.01 (2,1)
90/90/0/90/90	2.29 (2,1)	2.31 (2,1)	2.29 (2,1)	2.38 (2,1)	2.40 (2,1)	2.38 (2,1)
	$V^*_{CNT} = 0.17$					
0/0/90/0/0	8.92 (1,1)	8.97 (1,1)	8.88 (1,1)	9.27 (1,1)	9.33 (1,1)	9.24 (1,1)
0/90/0/90/0	8.92 (1,1)	8.97 (1,1)	8.88 (1,1)	9.27 (1,1)	9.33 (1,1)	9.24 (1,1)
90/0/90/0/90	7.60 (2,1)	7.67 (2,1)	7.57 (2,1)	8.97 (2,1)	9.05 (2,1)	8.93 (2,1)
90/90/0/90/90	3.51 (2,1)	3.54 (2,1)	3.51 (2,1)	3.64 (2,1)	3.68 (2,1)	3.65 (2,1)
	$V^*_{CNT} = 0.28$					
0/0/90/0/0	14.17 (1,1)	14.28 (1,1)	14.13 (1,1)	14.75 (1,1)	14.86 (1,1)	14.71 (1,1)
0/90/0/90/0	14.17 (1,1)	14.28 (1,1)	14.13 (1,1)	14.75 (1,1)	14.86 (1,1)	14.71 (1,1)
90/0/90/0/90	11.70 (2,1)	11.86 (2,1)	11.69 (1,1)	13.92 (2,1)	14.10 (2,1)	13.90 (2,1)
90/90/0/90/90	4.79 (3,1)	4.96 (3,1)	4.92 (3,1)	5.04 (3,1)	5.21 (3,1)	5.17 (3,1)

* The buckling mode (m,n)

Table 3 presents a significant difference in critical buckling compressive loads between non-corrugated FG-CNTRC and equivalent non-corrugated cores at different CNT volume fractions and distribution types, for both trapezoidal and round corrugation forms. As the CNT volume fraction increases, the load capacity of both core types increases; however, the critical buckling compressive loads of plates with corrugated core consistently show much higher values. Moreover, the differences between critical buckling loads of plates with corrugated and with equivalent non-corrugated cores are significant, ranging from 56.47% to 72.19%. The plates with trapezoidal corrugated cores with FG-X distribution show the highest critical buckling load in all three CNT volume fraction values. In addition, the round corrugated core also improves the critical buckling load of plates but is slightly lower than that of the trapezoidal corrugated core.

Table 3. Effects of the corrugated cores and the equivalent non-corrugated cores on the critical buckling compressions of FG-CNTRC plates (MPa) ($m=1$, $n=1$, $a=b=100h$, h_f=3mm, $h_c=15\text{mm}$, $f=2\text{mm}$, $c_t=4f$, $\theta=\pi/4$, $r=1.4\text{mm}$, $c_r=2r$, $d=0.6\text{mm}$, $t=1\text{mm}$, $T=400\text{K}$, $K_1=0\ \text{MN/m}^3$, $K_2=0\ \text{MN/m}$, $K_3=0\ \text{MN/m}^5$)

V^*_{CNT}	Trapezoidal corrugated cores			Round corrugated cores		
	UD	FG-X	FG-O	UD	FG-X	FG-O
			Corrugated core			
0.12	6.06 (71.45)**	6.10 (70.66)	6.04 (72.19)	6.31 (57.21)	6.34 (56.47)	6.28 (57.96)
0.17	8.92 (71.30)	8.97 (70.57)	8.88 (72.07)	9.27 (57.17)	9.33 (56.48)	9.24 (57.79)
0.28	14.17 (71.42)	14.28 (70.66)	14.13 (72.19)	14.75 (57.36)	14.86 (56.59)	14.71 (58.06)
			Equivalent non-corrugated core			
0.12	1.73	1.79	1.68	2.70	2.76	2.64
0.17	2.56	2.64	2.48	3.97	4.06	3.90
0.28	4.05	4.19	3.93	6.29	6.45	6.17

** The value difference between the corrugated core and equivalent non-corrugated core (%)

Fig. 3a examines the effects of CNT volume fraction on the postbuckling curves of FG-CNTRC plates with corrugated core under compressive loads, for both trapezoidal and round corrugations. The results indicate that increasing the CNT volume fraction enhances the postbuckling load-carrying capacity of the plates. Additionally, the compressive postbuckling curves for both corrugation forms show a clear increase trend, demonstrating stability in the postbuckling load-carrying capacity of the plates. Although both forms of corrugated cores show an increasing trend in postbuckling load-carrying capacity, the plates with trapezoidal corrugated cores achieve higher postbuckling load-carrying capacity. Fig. 3b shows that postbuckling pressure-carrying capacity increases as the CNT volume fraction increases for both perfect and imperfect cases.

Fig. 4 shows the effect of the thermal environment on the postbuckling load-carrying capacity of FG-CNTRC plates with trapezoidal and round corrugated cores. As the temperature increases, the postbuckling load-carrying capacity of the plates decreases significantly, indicating that higher temperatures reduce the load-carrying capacity of the plates. This reduction can be explained by the change in the thermal environment of the structures, which decreases their stiffness at higher temperatures. Additionally, the plates with round corrugated cores show higher postbuckling load-carrying capacity compared with the plates with the trapezoidal corrugated core at all temperatures.

Fig. 5 presents the relationship between postbuckling pressure curves with different pre-compressions for plates with the trapezoidal corrugated core. The results are presented for both perfect and imperfect plates. As the pre-compression increases, the pressure-carrying capacity also increases. Additionally, all curves display an upward trend in the postbuckling curve, indicating a better postbuckling pressure-carrying capacity in the large deflection region.

Figs. 6a and 6b present the effects of geometrical sizes of corrugated cores on the postbuckling compression-carrying capacity of FG-

CNTRC plates with trapezoidal and round corrugated cores, comparing perfect and imperfect plates. The results indicate that plates with trapezoidal corrugated cores have higher compression-carrying capacity than round corrugated ones. As the geometrical sizes of the corrugated cores increase, a reduction in postbuckling compression-carrying capacity is observed in both perfect and imperfect cases, showing that lower values for these sizes improve the load capacity of plates.

Fig 7a and 7b present the postbuckling curves of FG-CNTRC plates with trapezoidal corrugated core under axial compression load and round corrugated core under external pressure, with different a/h ratios, for perfect and imperfect plates. In both cases, the results show that as the a/h ratio increases, the load-carrying capacity of the plates decreases significantly, with the slopes of the curves becoming steeper in the large deflection region.

Fig 8a and 8b clearly demonstrate the effects of the linear foundation stiffnesses K_1, K_2 on the compressive load and external pressure for FG-CNTRC plates with trapezoidal and round corrugated cores. As the foundation stiffness increases, both the compressive load and external pressure increase significantly, thereby enhancing the load-carrying capacity of the plates. Moreover, in both subfigures, the difference between perfect and imperfect plates is also shown.

Fig. 9a and 9b present the effects of nonlinear foundation stiffness K_3 on the postbuckling curves of FG-CNTRC plates under compressive load and external pressure. Both scenarios involving positive and negative nonlinear stiffnesses of the foundation are illustrated. As depicted in Fig. 9a, the postbuckling curves of the plates exhibit a consistent upward trend when the nonlinear stiffness is positive. In contrast, when the nonlinear stiffness is negative, the postbuckling curves tend to decline in the region of large deflections. Fig. 9b also demonstrates a similar trend for plates under external pressure. As the positive values of K_3 increase, the load-carrying capacity increases accordingly, while the negative values of K_3 lead to a significant decrease in load-carrying capacity. These results indicate that the nonlinear foundation stiffness K_3 has a significant impact on the load-carrying capacity of the plates, particularly in the large deflection region.

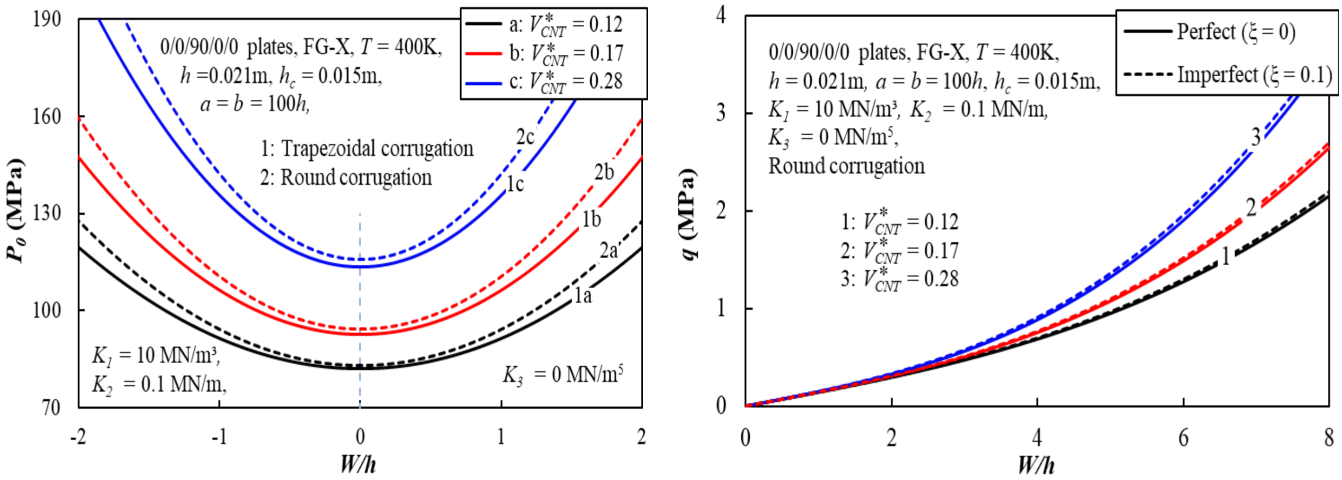

(a) (b)

Fig. 3. Effects of CNT distributions and volume fractions on the postbuckling behavior of plates with multi-layer corrugated core

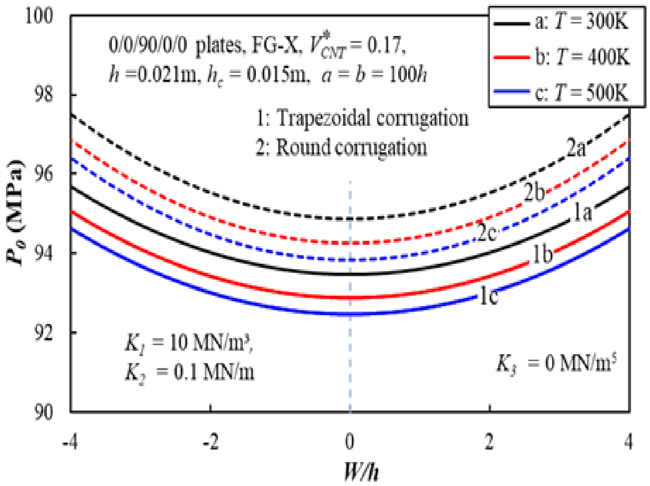

Fig. 4. Effects of thermal environment on the postbuckling curves of FG-CNTRC plates with multi-layer corrugated FG-CNTRC core

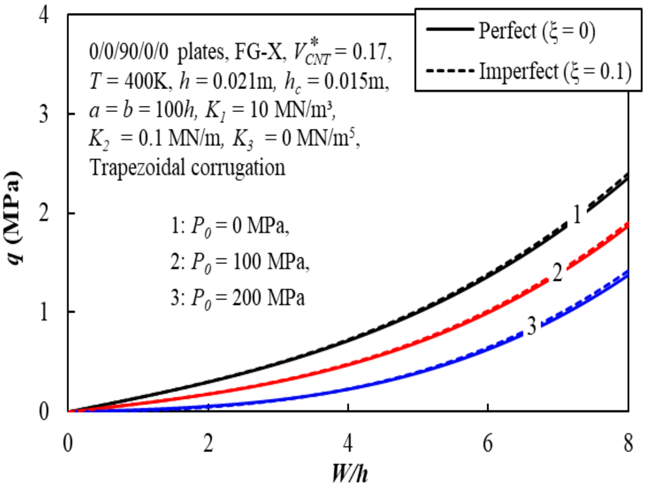

Fig. 5. Effects of the pre-compression on the postbuckling curves of FG-CNTRC plates with multi-layer corrugated FG-CNTRC core

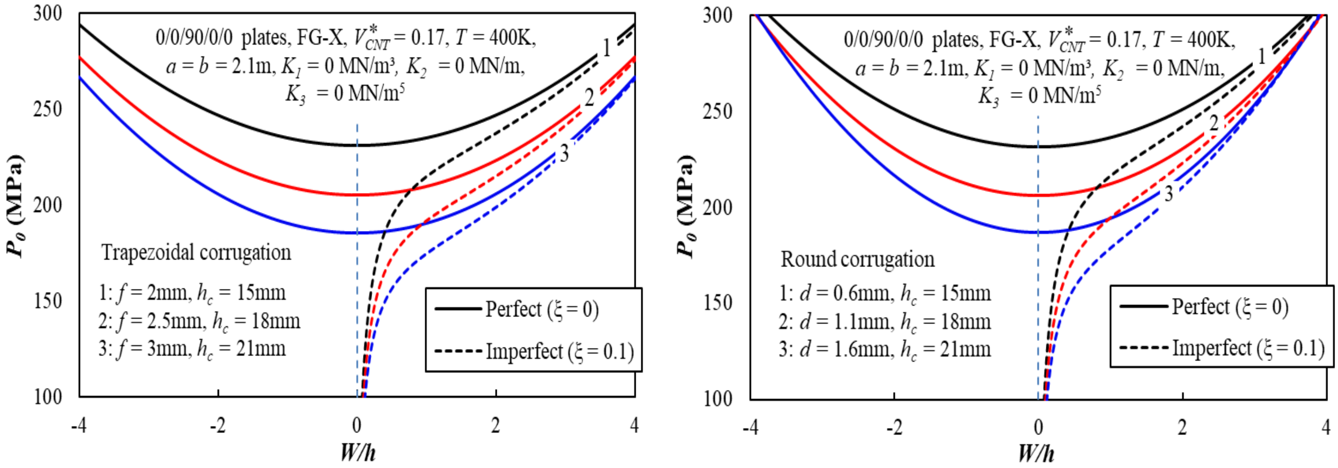

(a) (b)

Fig. 6. Effects of geometrical parameters of corrugated cores on the postbuckling curves of FG-CNTRC plates with multi-layer corrugated FG-CNTRC core

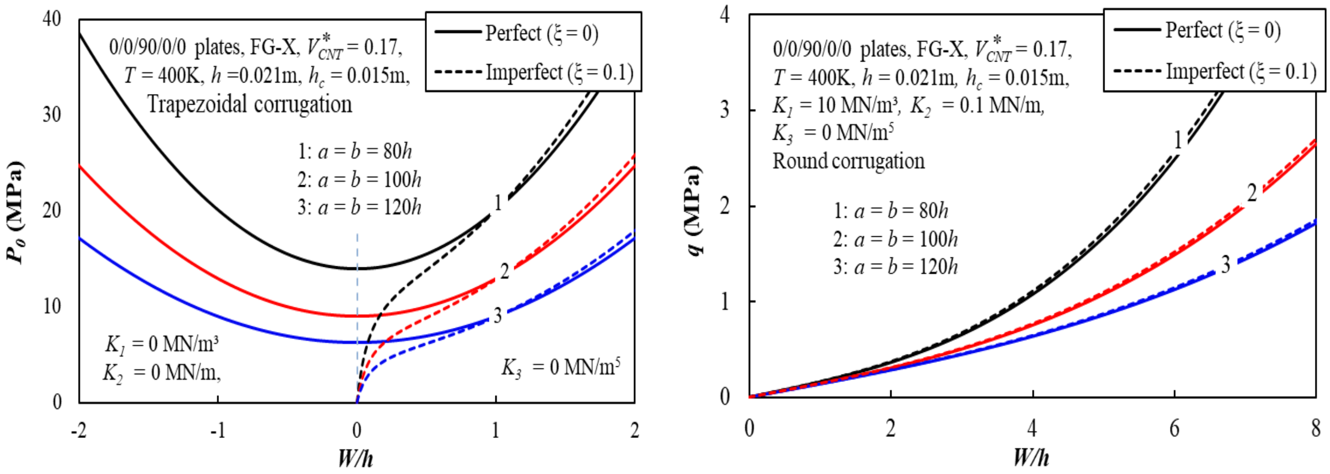

(a) (b)

Fig. 7. Effects of a/h ratio on the postbuckling curves of FG-CNTRC plates with multi-layer corrugated FG-CNTRC core

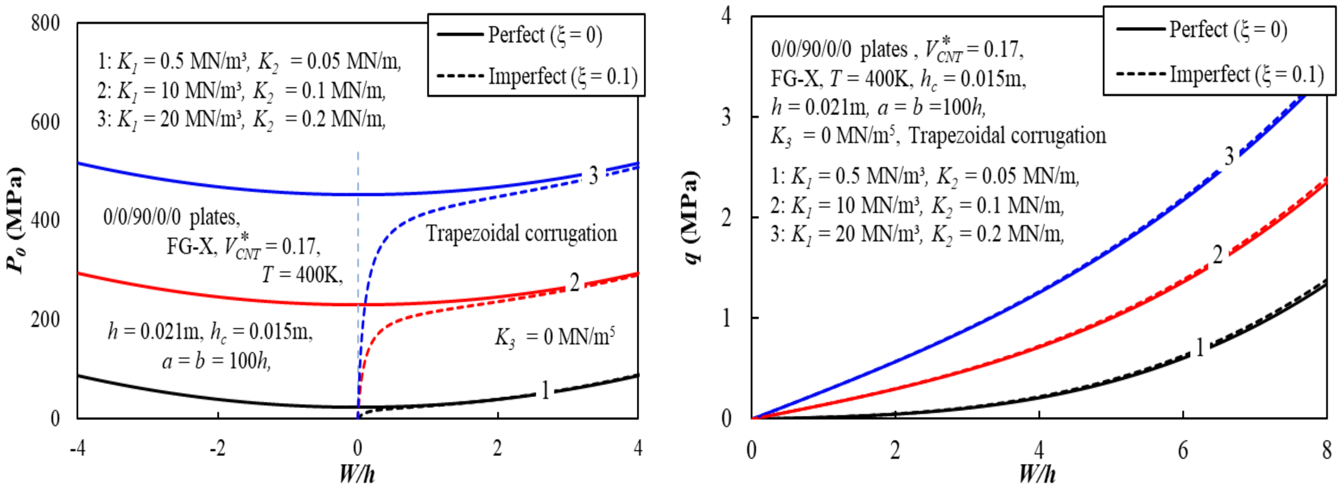

(a) (b)

Fig. 8. Effects of the linear foundation stiffnesses K_1, K_2 on the postbuckling curves of FG-CNTRC plates with multi-layer corrugated FG-CNTRC core

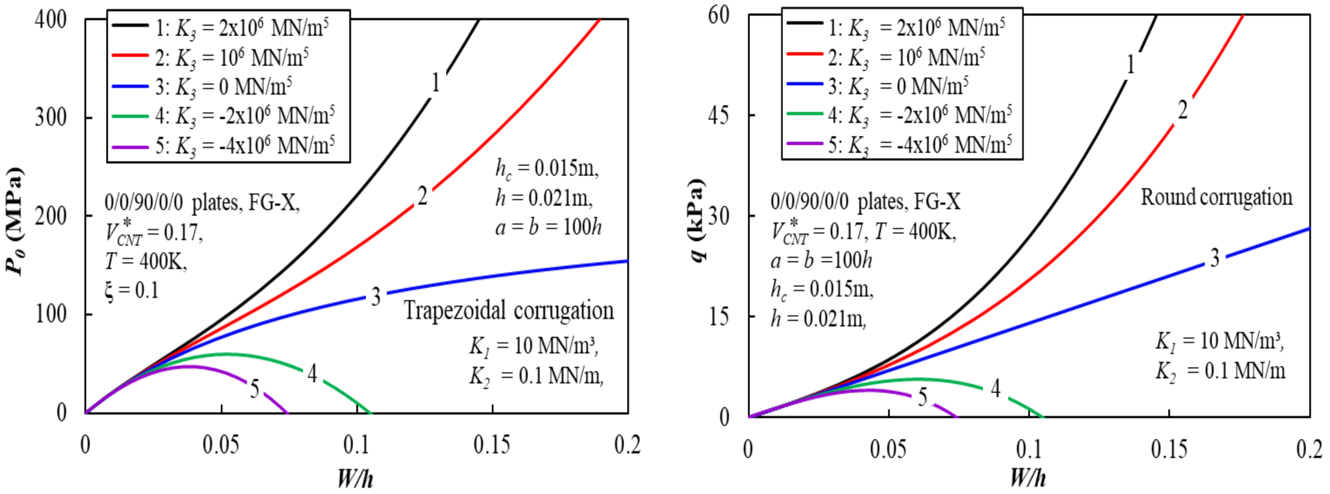

(a) (b)

Fig. 9. Effects of nonlinear stiffness of foundation K_3 on the postbuckling behavior of FG-CNTRC plates with multi-layer corrugated FG-CNTRC core

4. Conclusion

A formulation of governing equations of FG-CNTRC plates with multi-layer corrugated FG-CNTRC core based upon the CPT is presented in this paper. By using the energy method, and Xia et al.'s homogenization theory of corrugated structures, the explicit expressions of critical buckling loads and postbuckling load-deflection curve are obtained. From the numerical examples, some significant remarks can be obtained. The CNT volume fraction, directions of CNT in the face sheets and the corrugated core, and the distribution types of CNT and corrugation form have a significant effect on the postbuckling curves of FG-CNTRC plates. The FG-X distribution achieves the highest critical buckling load values, and the corrugated core demonstrates a significant superiority over the equivalent non-corrugated core, especially the round corrugated core. Additionally, environment temperature and foundation parameters also affect the load-carrying capacity of the plates.

References

[1] S.J. Singh, S.P. Harsha. (2019). Nonlinear dynamic analysis of sandwich S-FGM plate resting on pasternak foundation under thermal

environment. *European Journal of Mechanics - A/Solids,* 76, 155-179.

[2] M. Sobhy. (2016). An accurate shear deformation theory for vibration and buckling of FGM sandwich plates in hygrothermal environment. *International Journal of Mechanical Sciences*, 110, 62-77.

[3] A.M. Zenkour, M. Sobhy. (2010). Thermal buckling of various types of FGM sandwich plates. *Composite Structures*, 93, 93-102.

[4] N.V.D. Vuong, C.H. Lee. (2017). Thermal buckling analyses of FGM sandwich plates using the improved radial point interpolation mesh-free method. *Composite Structures*, 177, 171-186.

[5] D.T. Dong, D.V. Dung. (2019). A third order shear deformation theory for nonlinear vibration analysis of stiffened FGM sandwich doubly curved shallow shells with four material models. *Journal of Sandwich Structures and Materials*, 21(4), 1316-1356.

[6] V.H. Nam, N.T. Trung, L.K. Hoa. (2019). Buckling and postbuckling of porous cylindrical shells with functionally graded composite coating under torsion in thermal environment. *Thin-Walled Structures*, 144, 106253.

[7] V.H. Nam, N.T. Phuong, N.T. Trung. (2019). Nonlinear buckling and postbuckling of sandwich FGM cylindrical shells reinforced by spiral stiffeners under torsion loads in thermal environment. *Acta Mechanica*, 230, 3183-3204.

[8] H.S. Shen. (2009). Nonlinear bending of functionally graded carbon nanotube-reinforced composite plates in thermal environments. *Composite Structures*, 91(2), 9-19.

[9] Z.X. Lei, K.M. Liew and J.L. Yu. (2013). Buckling analysis of functionally graded carbon nanotube-reinforced composite plates using the element-free kp-Ritz method. *Composite Structures*, 98, 160-168.

[10] M. Wang, Z.-M. Li and P. Qiao. (2016). Semi-analytical solutions to buckling and free vibration analysis of carbon nanotube-reinforced composite thin plates. *Composite Structures*, 144, 33-43.

[11] H.S. Shen and Y. Xiang. (2014). Postbuckling of axially compressed nanotube-reinforced composite cylindrical panels resting on elastic foundations in thermal environments. *Composites Part B*, 67, 50-61.

[12] K.M. Liew, Z.X. Lei, J.L. Yu and L.W. Zhang. (2014). Postbuckling of carbon nanotube-reinforced functionally graded cylindrical panels under axial compression using a meshless approach. *Computer Methods in Applied Mechanics and Engineering*, 268, 1-17.

[13] M. Mohammadimehr, M. Mostafavifar. (2016). Free vibration analysis of sandwich plate with a transversely flexible core and FG-CNTs reinforced nanocomposite face sheets subjected to magnetic field and temperature-dependent material properties using SGT. *Composites Part B: Engineering*, 94, 253-270.

[14] H.S. Shen, H. Wang, D.Q. Yang. (2017). Vibration of thermally postbuckled sandwich plates with nanotube-reinforced composite face sheets resting on elastic foundations. *International Journal of Mechanical Sciences*, 124-125, 253-262.

[15] M. Di Sciuva, M. Sorrenti. (2019). Bending, free vibration and buckling of functionally graded carbon nanotube-reinforced sandwich plates, using the extended Refined Zigzag Theory. *Composite Structures*, 227, 111324.

[16] R. Ansari, J. Torabi, E. Hasrati. (2018). Axisymmetric nonlinear vibration analysis of sandwich annular plates with FG-CNTRC face sheets based on the higher-order shear deformation plate theory. *Aerospace Science and Technology*, 77, 306-319.

[17] N.N. Beni. (2019). Free vibration analysis of annular sector sandwich plates with FG-CNT reinforced composite face-sheets based on the Carrera’s Unified Formulation. *Composite Structures*, 214, 269-292.

[18] A.R. Setoodeh, M. Shojaee, P. Malekzadeh. (2019). Vibrational behavior of doubly curved

smart sandwich shells with FG-CNTRC face sheets and FG porous core. *Composites Part B: Engineering*, 165, 798-822.

[19] M. Wang, Z.M. Li, P. Qiao. (2018). Vibration analysis of sandwich plates with carbon nanotube-reinforced composite face-sheets. *Composite Structures*, 200, 799-809.

[20] Z.X. Wang, H.S. Shen. (2018). Nonlinear vibration of sandwich plates with FG-GRC face sheets in thermal environments. *Composite Structures*, 192, 642-653.

[21] A. Samanta and M. Mukhopadhyay. (1999). Finite element static and dynamic analysis of folded plates. *Engineering Structures*, 21(3), 277-287.

[22] L.X. Peng, K.M. Liew and S. Kitipornchai. (2007). Analysis of stiffened corrugated plates based on the FSDT via the mesh-free method. *International Journal of Mechanical Sciences*, 49(3), 364-378.

[23] T. Yokozeki, S. -I. Takeda, T. Ogasawara and T. Ishikawa. (2006). Mechanical properties of corrugated composites for candidate materials of flexible wing structures. *Composites Part A: Applied Science and Manufacturing*, 37(10), 1578-1586.

[24] P.T. Hieu, V.H. Nam, N.T. Phuong, L.T.N. Trang and V.T. Hung. (2016). Elastic stability of trapezoidal corrugated metal pipings subjected to external pressure. *Internal Journal of Science and Transport Technology*, 1, 17-22.

[25] S.W. Kavermann, D. Bhattacharyya. (2019). Experimental investigation of the static behaviour of a corrugated plywood sandwich core. *Composite Structures*, 207, 836-844.

[26] M. Shaban, A. Alibeigloo. (2017). Three-dimensional elasticity solution for sandwich panels with corrugated cores by using energy method. *Thin-Walled Structures*, 119, 404-411.

[27] C. Shu, S. Zhao, S. Hou. (2018). Crashworthiness analysis of two-layered corrugated sandwich panels under crushing loading. *Thin-Walled Structures*, 133, 42-51.

[28] H. Zamanifar, S. Sarrami-Foroushani, M. Azhari. (2019). Static and dynamic analysis of corrugated-core sandwich plates using finite strip method. *Engineering Structures*, 183, 30-51.

[29] Y. Xia, M. I. Friswell and E. I. Saavedra Flores. (2012). Equivalent models of corrugated panels. *International Journal of Solids and Structures*, 49(13), 1453-1462.

[30] V.H. Nam, D.T.K. My, V.M. Duc, L.N. Ly, N.T. Giang and N.T. Phuong. (2024). Nonlinear thermo-elastic stability of corrugated-core toroidal shell segments with carbon nanotube-reinforced face sheets under radial pressure. *Journal of Thermoplastic Composite Materials*, 37(6), 2100-2122.

[31] D.T.K. My, V.M. Duc, N.H. Giang, N.T. Phuong and V.H. Nam. (2024). Buckling and Postbuckling of Laterally Pressured Sandwich FG-GRC Laminated Toroidal Shell Segments with Corrugated Core in Thermal Environment. *International Journal of Structural Stability and Dynamics*, 24(04), 2450036.

[32] H.S. Shen. (2011). Postbuckling of nanotube-reinforced composite cylindrical shells in thermal environments, Part I: axially-loaded shells. *Composite Structures*, 93(8), 2096-2108.

[33] H.S. Shen. (2011). Postbuckling of nanotube-reinforced composite cylindrical shells in thermal environments, Part II: pressure-loaded shells. *Composite Structures*, 93(10), 2496-2503.

[34] H.S. Shen. (2014). Torsional postbuckling of nanotube-reinforced composite cylindrical shells in thermal environments. *Composite Structures*, 116, 477-488.

[35] H. Shen, Z.H. Zhu. (2010). Buckling and Postbuckling Behavior of Functionally Graded Nanotube-Reinforced Composite Plates in Thermal Environments. *Computers, Materials & Continua*, 18(2), 155-182.